Processing and Application of Ceramics 18 [1] (2024) 29–44
https://doi.org/10.2298/PAC2401029L

Cu and Er modified barium zirconium titanate ($BaZr_{0.05}Ti_{0.95}O_3$) ceramics: Composition-dependent dielectric properties

Aryan Singh Lather[1,*], Kanika Poonia[1], R.S. Kundu[1], Neetu Ahlawat[1], Anuj Nehra[1], Shubhpreet Kaur[2]

[1]*Department of Physics, Guru Jambheshwar University of Science & Technology, Hisar, 125001, Haryana, India*
[2]*Department of Physics, SLIET, Longowal, Sangrur, 148106, Punjab, India*

Received 21 August 2023; Received in revised form 12 December 2023; Accepted 4 February 2024

Abstract

Cu^{2+} and Er^{3+} doped $BaZr_{0.05}Ti_{0.95}O_3$ (BZT) ceramics were prepared using the solid-state reaction method, where amount of CuO + Er_2O_3 was fixed at 2 wt.% and different CuO : Er_2O_3 molar ratios (i.e. 1:1, 1:2, 1:3, 2:1 and 3:1) were used. The influence of Cu^{2+} and Er^{3+} doping on crystal structure and dielectric properties of the samples sintered at 1300 °C was investigated. X-ray diffraction analysis confirmed the formation of a single-phase material and tetragonal crystal structure with P4mm symmetry. Microstructural analysis conducted with a scanning electron microscope revealed well-defined and uniformly distributed grains across the surface of the sintered samples and reduction of grain size and density with doping. The highest energy storage density of 40.51 mJ/cm^3 with an energy efficiency of 78.8% was obtained in the sample with CuO : Er_2O_3 molar ratio of 2:1. The doped BZT ceramics have high dielectric constant and significantly lower tangent loss in comparison to the undoped BZT. The dielectric data confirm the non-Debye behaviour for all the samples. Impedance spectroscopy and electrical modulus analysis indicated that conduction in the materials was influenced by both the grains and grain boundaries. The AC conductivity is described by the Jonscher's universal power law, whereas DC conductivity follows a dependency based on the Arrhenius's theory. The results revealed a conduction mechanism characterized by non-overlapping small Polaron tunnelling up to 340 °C and a transition to correlated barrier hopping conduction above 340 °C within the selected temperature range for all the samples. According to the Arrhenius fitting of DC conductivity the activation energy of the undoped $BaZr_{0.05}Ti_{0.95}O_3$ sample is 0.168 eV and decrease with doping to 0.138 and 0.131 eV for the sample with lower Cu^{2+} contents (CuO : Er_2O_3 molar ratios of 1:2 and 1:3, respectively).

Keywords: *doped $BaZr_{0.05}Ti_{0.95}O_3$, structure, conductivity, dielectric property, impedance spectroscopy*

I. Introduction

Lead-free ceramics with a perovskite structure (ABO_3), such as NBT, KNN, BNT and barium titanate, have attracted considerable attention due to environmental concerns [1–7]. These ceramics find wide applications in electronics, including RAMs, actuators and MLCCs. Particularly, barium zirconium titanate ($BaZr_xTi_{1-x}O_3$), known for its customizable electrical and optical characteristics, has intrigued researchers. The material demonstrates favourable electrical characteristics, including a moderate dielectric constant and low dielectric dissipation factor, which make it well-suited for applications in ceramic capacitors and RAMs [8–12]. $BaZr_xTi_{1-x}O_3$ system displays composition-dependent polymorphic phase transitions [13–15]. As the percentage of Zr increases in $BaZr_xTi_{1-x}O_3$, the polymorphic phase transitions, including rhombohedral to orthorhombic, orthorhombic to tetragonal, and tetragonal to cubic, converge on each other. This leads to a shift from ferroelectric to paraelectric at lower temperatures and other transitions shifting to higher temperatures. Interestingly, these transitions occur near ambient temperature for a specific composition of $BaZr_xTi_{1-x}O_3$

*Corresponding author: tel: +91 9466962130
e-mail: *aryansinghlather@gmail.com*

with x = 0.15 [16,17]. After an extensive literature review, we have come across encouraging results regarding $BaZr_{0.05}Ti_{0.95}O_3$ in terms of its piezoelectric, electrostrictive strain, ferroelectric and luminous properties [18–21].

The incorporation of rare earth ions (Re^{3+}) into the $BaZr_xTi_{1-x}O_3$ system has attracted considerable attention in research circles owing to their remarkable electrical characteristics [22–24]. These Re^{3+} ions can influence lattice symmetry and grain size, which are crucial factors in studying electrical properties [25–33]. Some researchers have explored the doping of $BaTiO_3$ with Er^{3+} [30,34,35]. Among various rare earth ions, Er^{3+} doping introduces multifunctional properties to the system [30]. Furthermore, electrical measurements revealed that in Er^{3+} based $BaTiO_3$ conduction mechanism is either an NSPT (Non-overlapping Small Polaron Tunnelling) or a CBH (Correlated Barrier Hopping) model [30]. Similarly, the effect of Cu-doping on $BaTiO_3$-based ceramics has been studied several times [33–36]. Studies showed that Cu increases electric conductivity of $BaZr_xTi_{1-x}O_3$ and exhibits a temperature-dependent relaxation phenomenon. In a nutshell, Er^{3+} or Cu^{2+} doped barium titanate exhibits changes in the microstructure and improves electrical, magnetic and optical properties.

It is important to underline that $BaZr_xTi_{1-x}O_3$ material with Er_2O_3 and CuO addition has not been explored yet. Therefore, to improve electrical characteristics, we used Er^{3+} and Cu^{2+} ions in various molar ratios to substitute in $BaZr_{0.05}Ti_{0.95}O_3$ (BZT) ceramics with total CuO + Er_2O_3 amount of 2 wt.% [37]. It is assumed that small Cu^{2+} ion will substitute Ti^{4+} at B-site, however larger Er^{3+} can be introduced preferable on both A-site but could be also at B-site. The structural, microstructural, dielectric and impedance behaviour of $BaZr_{0.05}Ti_{0.95}O_3$ ceramics doped with Eu^{3+} and Cu^{2+} ions has been the focus of our research.

II. Experimental

Eu^{3+} and Cu^{2+} doped $BaZr_{0.05}Ti_{0.95}O_3$ powders were synthesized using a solid-state reaction method and Ba_2CO_3, ZrO_2 and TiO_2 (Sigma Aldrich) powders in stoichiometric proportions. The initial step involved mixing the raw powders in a mortar and pestle for duration of 6 h. The mixture was then calcined at 1100 °C for 5 h in a high-temperature furnace. The calcined $BaZr_{0.05}Ti_{0.95}O_3$ powder was combined with varying molar ratios of CuO to Er_2O_3, and the amount of CuO + Er_2O_3 was fixed at 2 wt.%. The resulting mixtures were further ground in a mortar and pestle for 2 h. The CuO : Er_2O_3 molar ratios were adjusted to 1:1, 1:2, 1:3, 2:1 and 3:1. The dopant content and abbreviations used throughout the manuscript are given in Table 1. To form cylindrical pellets, 2.5 wt.% PVA binder was added to the mixed powders and hydraulic pellet pressing was performed at uniaxial pressure of 100 MPa. Subsequently, the obtained pellets were sintered at 1300 °C for 6 h. Throughout the manuscript, the

Table 1. Abbreviations and dopant content

Abbreviation	CuO + Er_2O_3 amount [wt.%]	CuO to Er_2O_3 molar ratio
BZT	0	-
CE	2	1:1
CE2	2	1:2
CE3	2	1:3
2CE	2	2:1
3CE	2	3:1

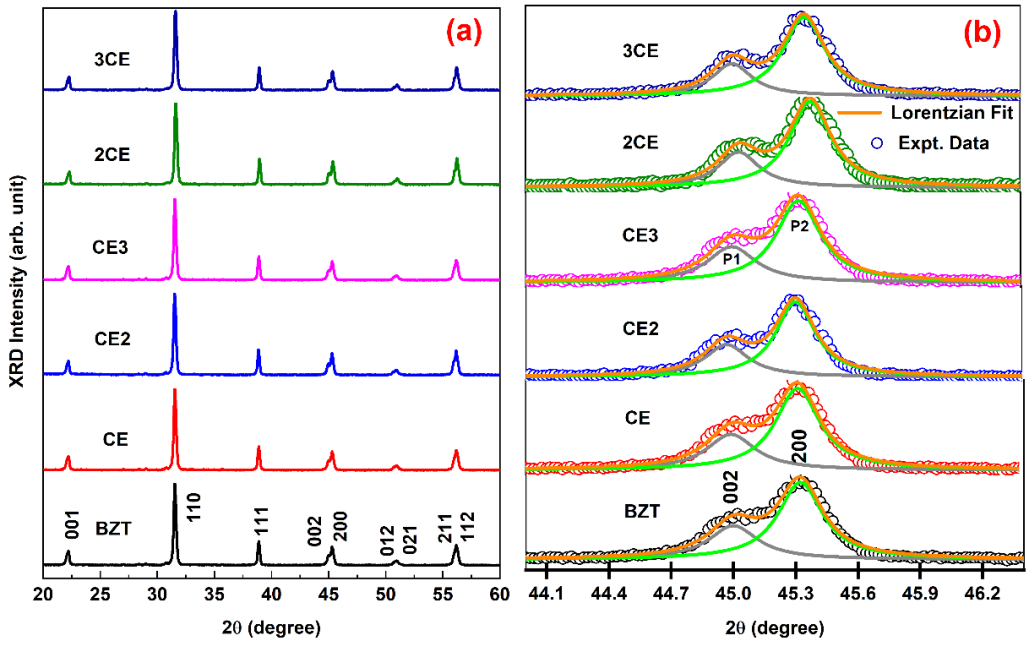

Figure 1. XRD patterns of BZT, CE, CE2, CE3, 2CE and 3CE ceramics (a) and the Lorentzian fit of the reflected peak at 45.32° (b)

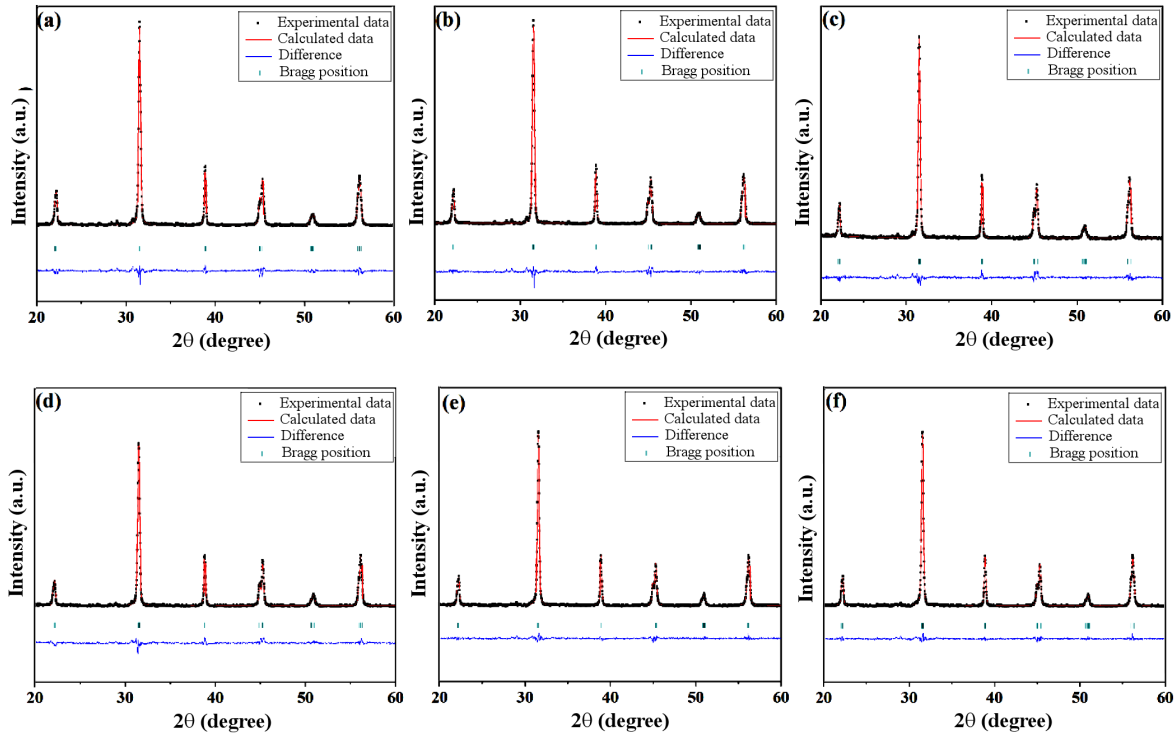

Figure 2. The refined XRD patterns for sintered ceramics: a) BZT, b) CE, c) CE2, d) CE3, e) 2CE and f) 3CE

sintered samples will be also referred to by their respective names for simplicity.

To analyse the initial phase of the samples, XRD data were collected on Rigaku Miniflex-II with Cu-K radiation. The microstructures of the ceramics were examined using a FESEM (JEOL JSM-7610FPlus), while density measurements were performed using the Denver Instrument SI-234. FTIR spectra were measured using a spectrometer from Perkin Elmer. Furthermore, the ferroelectric properties were investigated using a *P-E* loop tracer. The measurement of dielectric properties and complex impedance were measured using a Novo control Alpha A Impedance Analyser.

III. Results and discussion

3.1. Structural analysis

XRD patterns of the sintered BZT, CE, CE2, CE3, 2CE and 3CE samples are displayed in Fig. 1a. Preliminary visual analysis of the diffractograms revealed that the XRD peak at 38.7° is a singlet and the 45.3° peak is doublet in nature (Fig. 1b). This suggests the presence of a distorted perovskite with a tetragonal-like structure, considering that the undoped BZT sample possesses tetragonal crystal structure [38]. To further investigate the crystal structure, the Rietveld refinement analysis was conducted using the tetragonal structure model with the *P*4*mm* phase group. The refined XRD patterns of all the samples are presented in Fig. 2. The Rietveld analysis revealed that all samples exhibit a good fit to the tetragonal phase with *P*4*mm* symmetry. The refined parameters for each sample are presented in Table 2.

The refined XRD parameters provide important insights into the crystal structure of the doped samples. The presence of the tetragonal phase with *P*4*mm* symmetry suggests successful doping and incorporation of the desired elements into the perovskite lattice. The observed variations in lattice constants further confirm the effect of doping elements on the crystal structure, emphasizing the role of atomic size differences in determining these changes.

There is a minor peak shift observed with increasing erbium and copper content. This shift can be attributed to the mismatch in ionic radii of the doping elements. The larger size of Cu^{2+} (73 pm) and Er^{3+} (89 pm) ions compared to Ti^{4+} (56 pm) at the B site induces lattice expansion [39], as evidenced by the observed changes in lattice parameters (a and c) documented in Table 2. The unit cell dimensions (a, b, c) and angle β show slight variations among the samples, but they remain relatively close in value. This suggests that the doping does not significantly alter the overall crystal lattice. However, the variation in parameters with an increase in Er concentration (the samples CE2 and CE3) is more pronounced than for the samples with higher Cu content (the samples 2CE and 3CE). The volume of the unit cell remains almost consistent across the samples, indicating similar unit cell sizes, but somewhat higher cell volume has the samples with higher Er content (the samples CE2 and CE3). The c/a ratio, which represents the elongation along the c-axis, shows a slight elongation in all the samples. It has been observed (Table 2) that the value of χ^2 is less than 5 for each sample. This indicates that experimental and theoretical data have a very strong

Table 2. The refined parameters, including the calculated average grain size (D) and experimental density (ρ) for the sintered samples

Sample	BZT	CE	CE2	CE3	2CE	3CE
Space Group	*P4mm* (tetragonal)	*P4mm* (tetragonal)	*P4mm* (tetragonal)	*P4mm* (tetragonal)	*P4mm* (tetragonal)	*P4mm* (tetragonal)
a [Å]	4.0022	4.0026	4.0035	4.0064	4.0013	4.0015
b [Å]	4.0022	4.0026	4.0035	4.0064	4.0013	4.0015
c [Å]	4.0297	4.0300	4.0325	4.0355	4.0304	4.0308
β [°]	90	90	90	90	90	90
V [Å^3]	64.54	64.56	64.63	64.77	64.52	64.54
c/a	1.0069	1.0068	1.0072	1.0073	1.0073	1.0073
D [μm]	36.1	16.7	11.9	13.6	12.4	10.6
ρ [g/cm^3]	6.60	6.56	6.53	6.49	6.58	6.55
R_{wp}	5.0	5.09	5.43	5.61	6.11	5.89
χ^2	4.1	4.23	4.69	4.38	4.10	3.89

correlation. The characteristic XRD peaks shown in Fig. 1b were deconvoluted using the Lorentzian multi-peak fit, employing the phase information acquired from Rietveld refinement. A good agreement with the experimentally obtained XRD data indicates the presence of a pure phase.

3.2. Microstructure characterization

The micrographs captured from FESEM (Fig. 3) reveal a gradual reduction in grain size in the doped samples. To quantitatively determine the grain size, the ImageJ software was employed and the obtained data was visualized through histogram plots (insets in Fig. 3). Fitting by the Gaussian function was used to calculate the average grain sizes. These data together with experimental density values of the sintered ceramics are tabulated in Table 2.

The data indicate that the growth of grains is limited, which could be attributed to the presence of doping elements leading to the precipitation of larger Er/Cu ions at the grain boundary. It seems that Er^{3+} exhibited a more pronounced influence on the grain size compared to Cu^{2+}. This can be attributed to the difference in valence state of Er and Cu as well as ionic radii of Er^{3+} and Ba^{2+} as compared to Cu^{2+} and Ti^{4+} (Er^{3+} = 89 pm, Ba^{2+} = 161 pm, Cu^{2+} = 73 pm, Ti^{4+} = 56 pm). Furthermore, the density values of the samples exhibited good correlation with the observed grain size values, i.e. the greater the grain size, the higher is the density. Thus, the samples exhibiting relatively larger grain size have higher density.

3.3. FTIR analysis

The characterization of functional groups in the samples was conducted using the Fourier transform infrared (FTIR) technique. Several distinguishable bands, that provide valuable information about the sample composition, are clearly seen in the spectra (Fig. 4). The

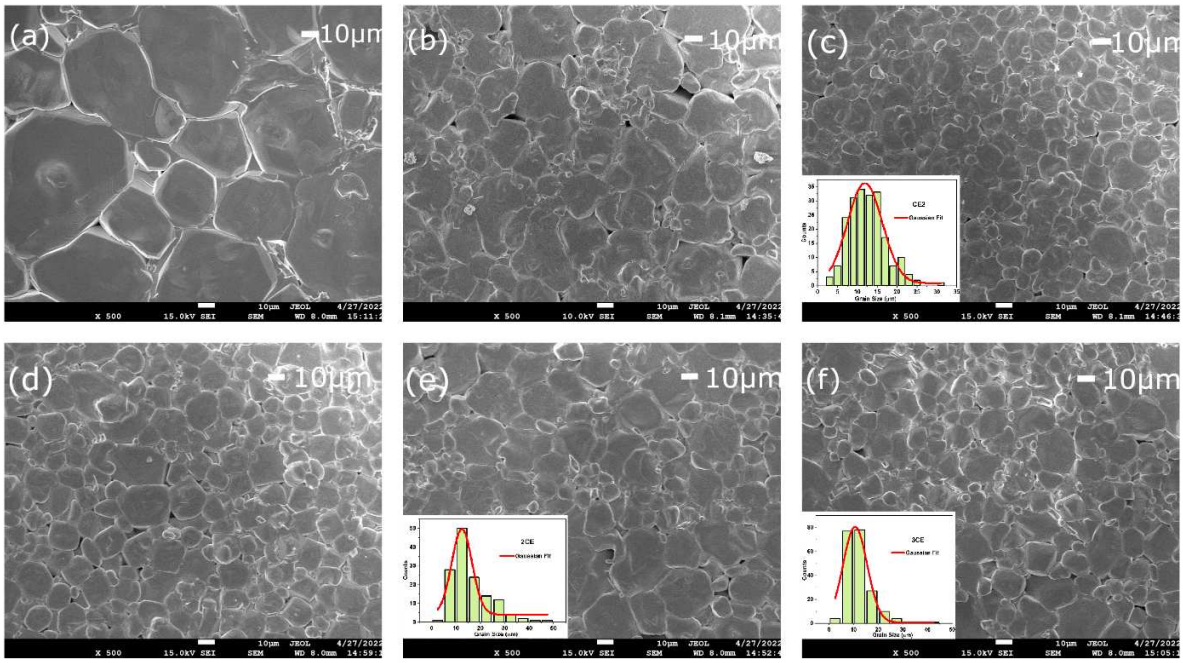

Figure 3. FESEM micrographs of samples: a) BZT, b) CE, c) CE2, d) CE3, e) 2CE and f) 3CE

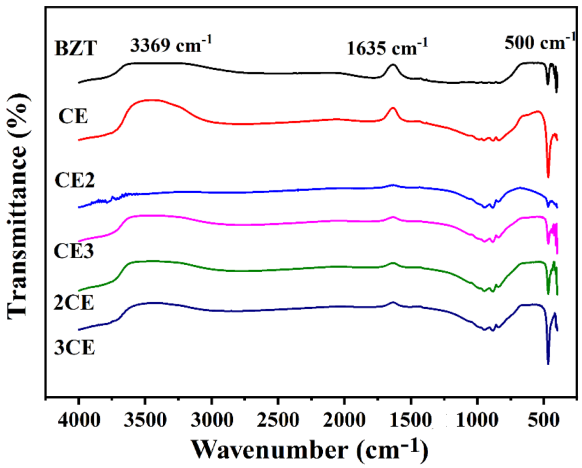

Figure 4. FTIR results for sintered samples

broad band observed at 3369 cm^{-1} is related to expansion of the O–H bond [40,41]. Another significant feature detected in the FTIR spectra is the presence of a band at 1635 cm^{-1}, which can be assigned to the Cu–O bond [40]. The vibrations associated with the Zr–O, Ti–O, Er–O and Cu–O bonds contribute to a distinct band ranging from 500 to 490 cm^{-1} [40,42]. A prominent peak observed around 500 cm^{-1} is of particular interest and is consistently present in all samples. This peak is indication of tetragonal structure of the doped $BaZr_{0.05}Ti_{0.95}O_3$. Its consistent appearance across different samples strengthens the hypothesis that the desired tetragonal structure has been successfully obtained [43,44]. This observation confirms that the FTIR results align with the structural information provided by XRD.

3.4. Dielectric properties

Figures 5 and 6 depict a typical frequency-dependent variation of the relative dielectric constant (ε') and dielectric loss ($\tan\delta$) for various samples. The pattern of fluctuation demonstrates that ε' and $\tan\delta$ both drop as frequency rises, characteristic behaviour of dielectric or ferroelectric materials. The samples demonstrate the presence of multiple polarizations at room temperature, encompassing electronic, ionic, dipolar and interfacial polarizations. These diverse polarizations contribute to the elevated value of ε' at low frequencies [45]. On the other hand, at higher frequencies only electronic polarization dominates, leading to lower values of ε'. Moreover, with the variation in composition, there is only a small difference in all the samples. In comparison to the BZT ceramics, a small increase of the Curie temperature as well as a slight increase in diffusivity is observed in the Er/Cu doped samples (Fig. 5). The doped BZT ceramics exhibit also increased dielectric constant and a significant reduction in tangent loss. This phenomenon can be attributed to the substitution of ions with larger ionic radii, such as Er^{3+} (89 pm) and Cu^{2+} (78 pm) on the Ti^{4+} (63 pm) site. This substitution restricts the movement of ions, resulting in a reduced sensitivity to temperature variations. This distribution of local Curie points and microscopic heterogeneity contributes to the observed diffusivity in ε' versus temperature plots, as depicted in Figs. 5d,e,f.

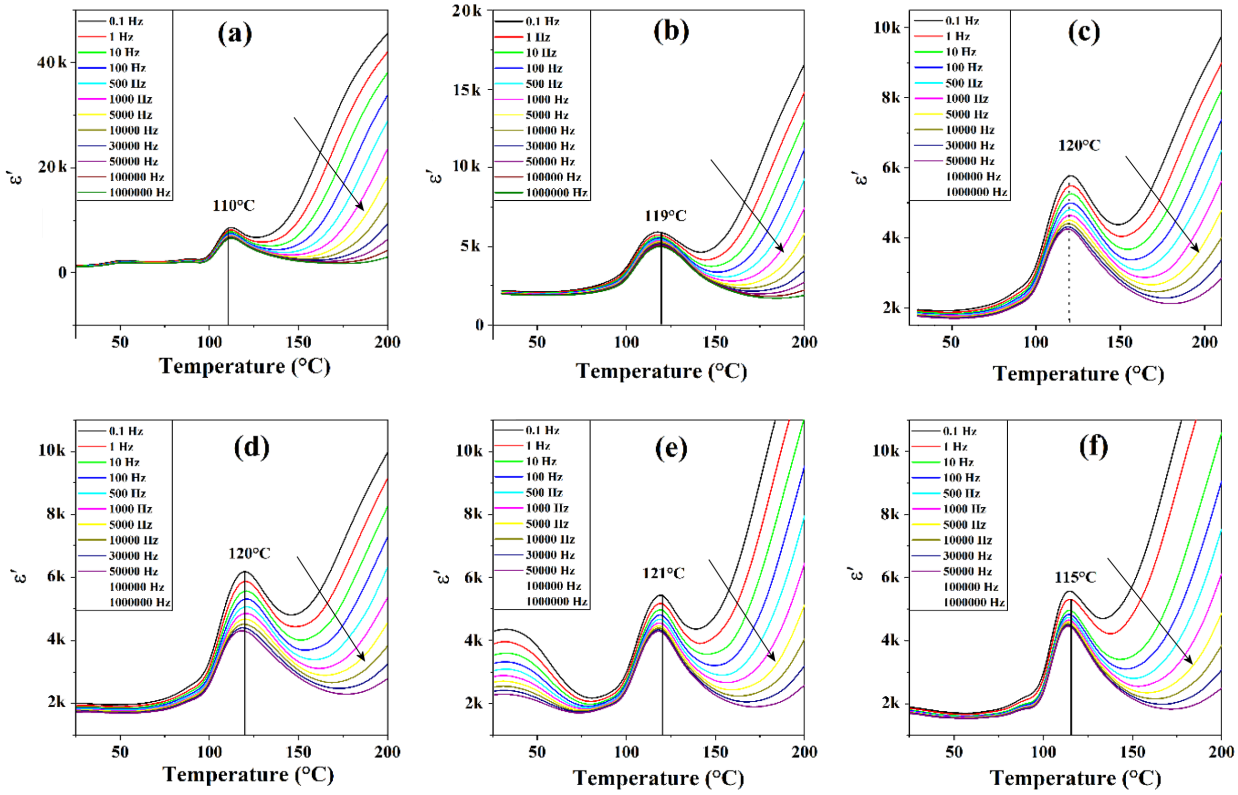

Figure 5. ε' vs. temperature profile for samples: a) BZT, b) CE, c) CE2, d) CE3, e) 2CE and f) 3CE

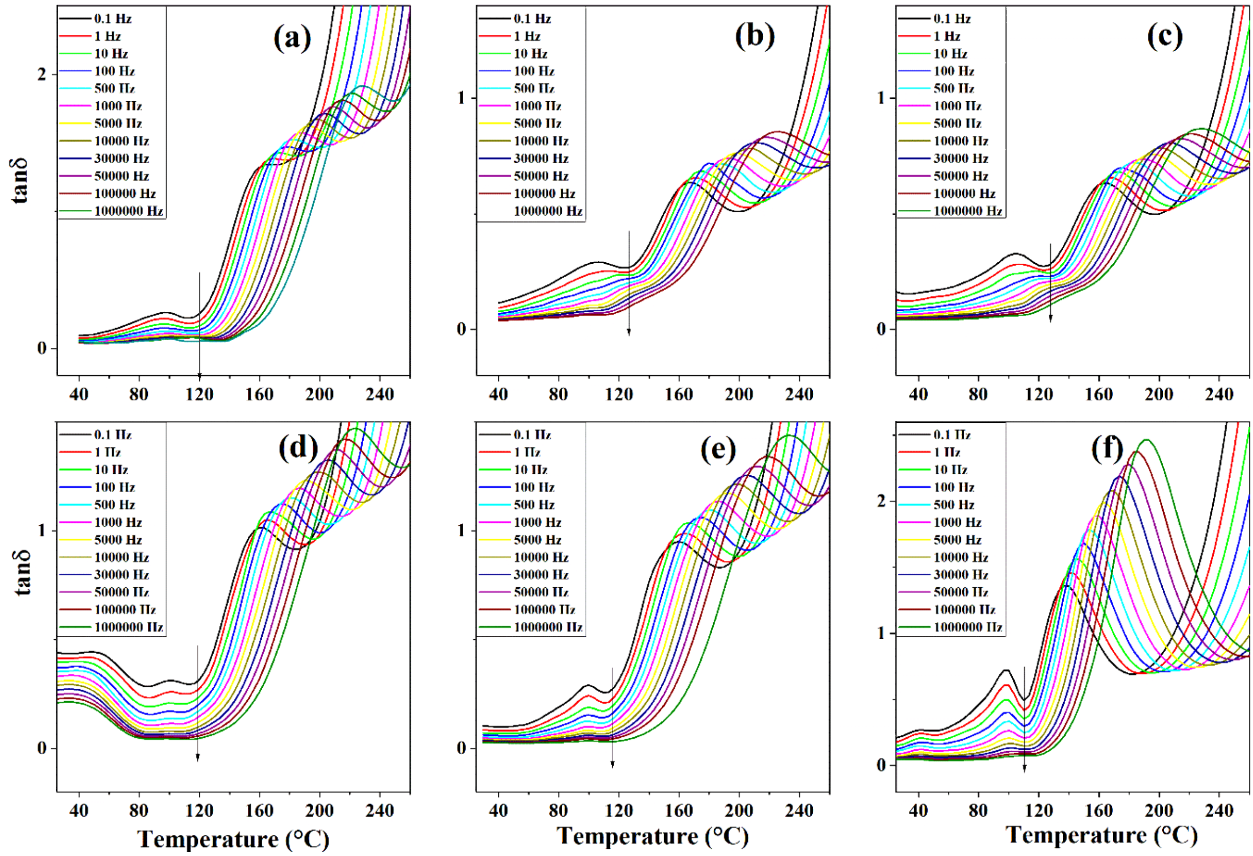

Figure 6. tanδ vs. temperature profile for samples: a)BZT, b) CE, c) CE2, d) CE3, e) 2CE and f) 3CE

3.5. Ferroelectric properties

Figure 7 illustrates the hysteresis loops of the sintered ceramics at ambient temperature. The ferroelectric polarization observed in the material is attributed to the hybridization of titanium and oxygen ions in the 3*d* and 2*p* states [46,47]. In the case of the doped BZT ceramics, *P-E* loop displays unsaturated loops. This behaviour could also indicate the existence of a magnetic phase in the composite. Similar characteristics were reported by Kumar *et al.* [48]. Additionally, the number of grain boundaries increases as the grain size decreases, which influences the ferroelectric properties. The polarization can be affected by the depolarizing field caused by the accumulation of space charge on grain boundaries, which prevents polarization charge on grain surface [49]. Ceramics with larger grain sizes tend to exhibit higher residual polarization P_r and lower coercive field E_C values [50]. The variable oxidation state of Cu introduces electronic heterogeneity, which affects conductivity, oxygen concentration and polarization of the material [50]. Notably, all doped samples demonstrated a gradual increase in residual polarization and coercive field compared to the BZT ceramics (Table 3).

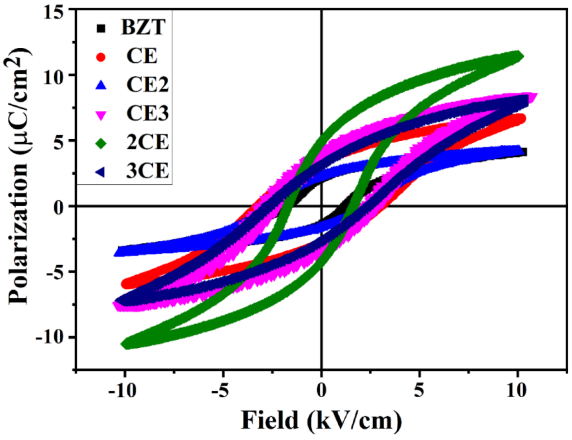

Figure 7. The hysteresis loops for each sample at room temperature

The polarization values of the modified BZT materials experience a significant increase due to Er^{3+}/Cu^{2+} doping, which causes a charge imbalance. The CE2 sample exhibits the lowest polarization value of 2.21 μC/cm^2, closely to the BZT sample with P_r = 2.13 μC/cm^2 (Table 3). The 2CE sample demonstrates the highest maximum polarization of 4.94 μC/cm^2 and the lowest coercive field value of 1.64 kV/cm among all doped samples, indicating its ability to switch polarity with less applied electric field, which aligns with values reported in the literature for BZT-based materials.

The energy storage density was determined using the following equation:

$$W = \int_{P_r}^{P_{max}} E \cdot \mathrm{d}P \qquad (1)$$

Table 3. Remnant polarization, coercive fields, energy density and efficiency for all the samples

Sample	Polarization [μC/cm^2]	Coercive field [kV/cm]	Energy density [mJ/cm^3]	Efficiency, ξ [%]
BZT	2.13	1.17	6.709	39.4
CE	3.32	3.08	12.87	32.1
CE2	2.21	2.24	18.68	39.7
CE3	3.65	2.62	13.57	65.9
2CE	4.94	1.64	40.51	78.8
3CE	3.29	2.20	16.39	39.9

where E represents the applied electric field, P_{max} denotes maximum polarization and P_r signifies the remnant polarization. Table 3 also presents the calculated energy storage efficiency (ξ). The storage efficiency (ξ) in case of the 2CE sample exhibits the highest storage efficiency, reaching an impressive 78.8%. This indicates its ability to efficiently store and release energy. The CE3 sample also demonstrates high efficiency with a storage efficiency of 65.9%.

These results show the enhanced polarization properties of the modified BZT ceramics, highlighting the sample 2CE standing out as a promising option for high-energy applications. The obtained results contribute to the understanding and potential of optimizing ferroelectric materials for various technological advancements.

3.6. Complex impedance analysis

Figure 8 illustrates how the actual impedance component (Z') varies with frequency at various temperatures (between 300 and 400 °C). At low frequencies, Z' is large and decreases with increasing frequency, exhibiting the characteristic NTCR (negative temperature coefficient of resistance) [51]. Based on the decreasing tendency of Z' with rising temperature and frequency values, AC conductivity may rise with temperature [52,53]. The decrease in Z' at all temperatures indicates the discharge of space charge in the high-frequency region and a reduction in the material's barrier properties. This phenomenon weakens the impedance and allows for easier charge flow through the material [54,55].

Figure 9 shows the change of Z'' (imaginary part of impedance) versus frequency at different temperatures. As temperature and frequency rise, the magnitude of Z'' drops, implying that the material's resistive properties have degraded. The noticeable broadening of the peaks with increasing temperature suggests that the electrical relaxation phenomenon in the material is influenced by changes in temperature. Immobile species or electrons can produce relaxations at low temperatures, whereas vacancies or defects can induce relaxation at high temperatures [51,52,56]. Moreover, the disappearance of space-charge polarisation could cause the convergence of all curves at higher frequencies [57,58]. The observed peaks in the imaginary component (Z'') of impedance, corresponding to different frequencies, in the doped $BaZr_{0.05}Ti_{0.95}O_3$ (BZT) ceramics can be understood by considering the complex impedance response of the material. These peaks and their shifting heights towards

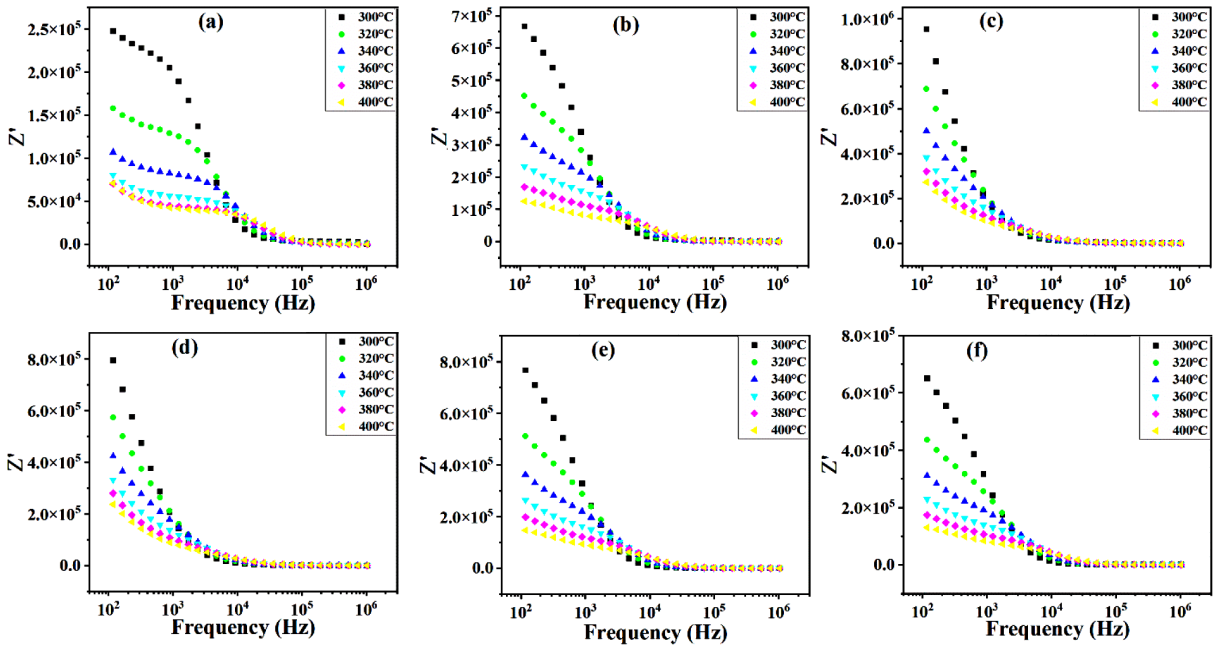

Figure 8. The real component (Z') of impedance with respect to frequency for samples: a) BZT, b) CE, c) CE2, d) CE3, e) 2CE and f) 3CE

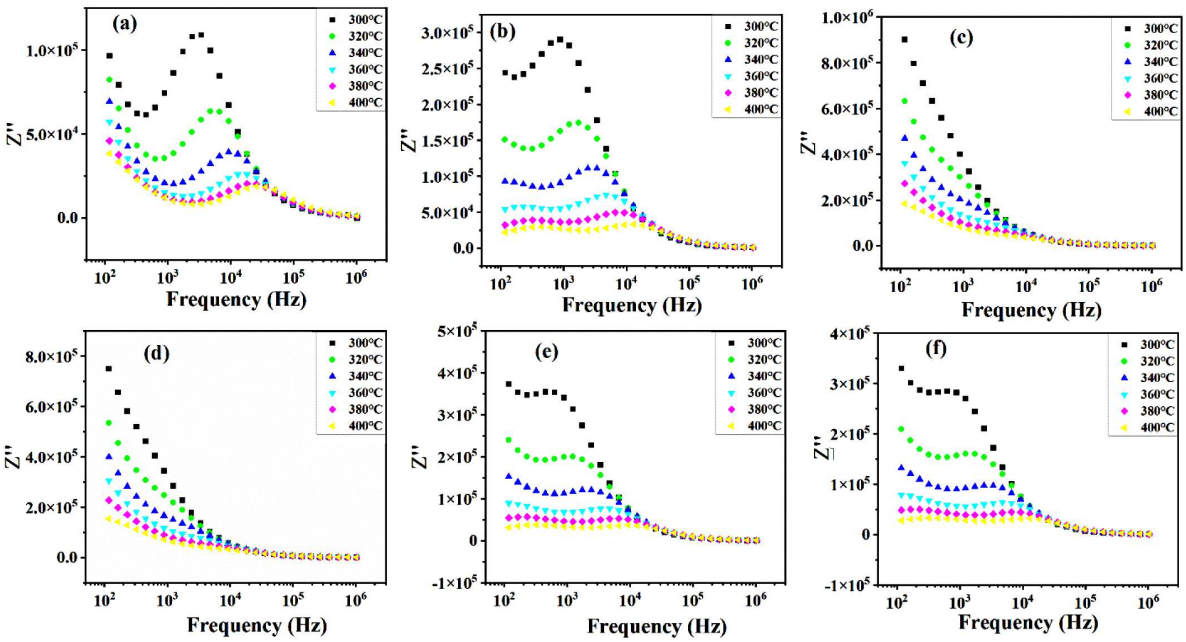

Figure 9. The imaginary component (Z'') of impedance with respect to frequency for samples: a) BZT, b) CE, c) CE2, d) CE3, e) 2CE and f) 3CE

higher frequencies can be attributed to the impact of Er^{3+} and Cu^{2+} dopants on the electrical and structural properties of the BZT ceramic. The doping changes the crystal lattice of a ceramic material such as BZT by introducing defects, which can create localized electronic states and influence the movement of charge carriers.

At certain frequencies, corresponding to the characteristic relaxation times of the defects, the movement of charge carriers becomes impeded or restricted, leading to increased resistance and enhanced imaginary impedance. This causes appearance of a peak in the Z'' curve. The shifting of peak heights towards higher frequencies can be attributed to the modification of the dopant concentrations. Different molar ratios of CuO to Er_2O_3 introduce varying defect densities and distribution within the BZT ceramics. This affects the energy barrier heights and relaxation times associated with the charge carrier movement. By altering the dopant ratios, the concentration and nature of the introduced defects change, leading to a shifting of the peak heights towards higher frequencies. This indicates that the dopants' molar ratio and their impact on the defect structure of BZT

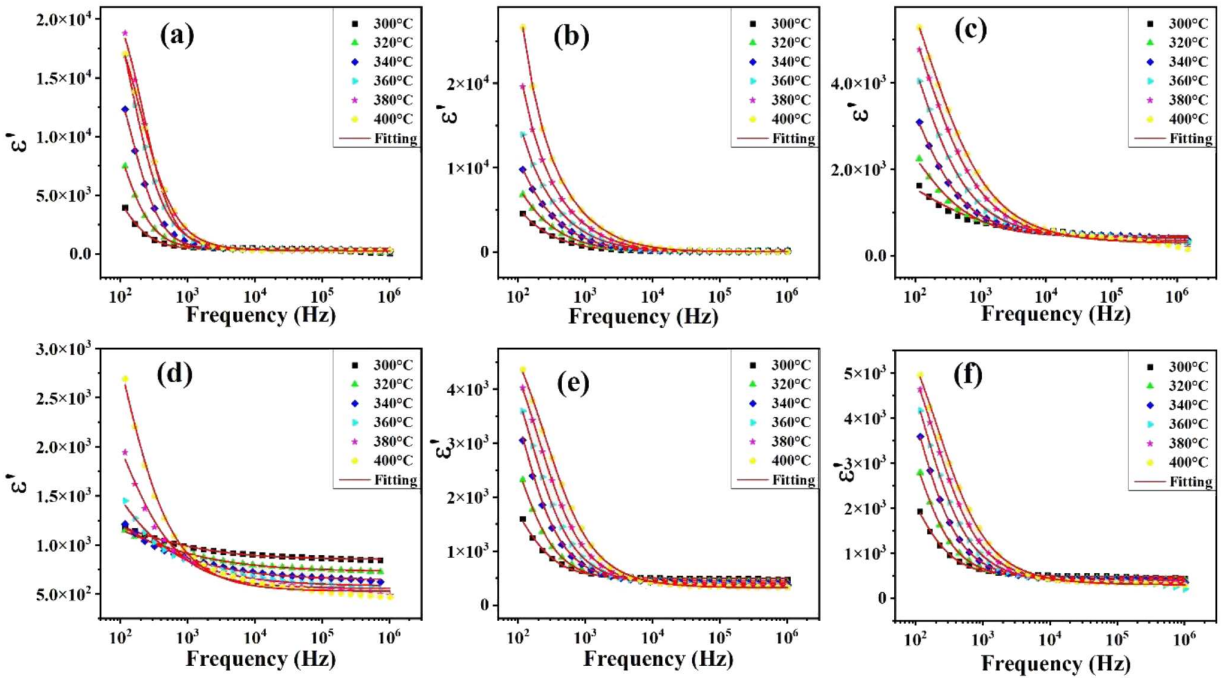

Figure 10. The profile of Z'' vs Z' (the Nyquist plot) for samples: a) BZT, b) CE, c) CE2, d) CE3, e) 2CE and f) 3CE

play a crucial role in determining the impedance response and the position of the peaks in the Z'' component.

Figure 10 shows Z'' vs. Z' profile (the Nyquist plots) and frequency domain fitting results at different temperatures ranging from 300 to 400 °C. The presence of a semicircle with its centre below the real axis indicates non-Debye behaviour, which can be explained by various parameters such as atomic defect distribution, grain orientation, grain boundaries, and stress-strain mechanisms [51]. Moreover, the material demonstrates a negative temperature coefficient of resistance (NTCR) behaviour, where the radius decreases as the temperature rises. The impedance curves, predominantly influenced by grain and grain boundary conduction, are typically simulated using the ZView software with a perfect analogue circuit [52,59]. The network consists of several components [60,61], i.e. the corresponding equivalent circuit is shown in inset of Fig. 10a. The grain circuit is composed of parallel resistance (R_g) and capacitance (CPE_g), while the grain boundaries consist of parallel R_{gb} and CPE_{gb} pairs. However, the constant phase component (CPE) deviates from the ideal Debye model scenario. CPE's impedance is determined by $Z_{CPE} = 1/(i\omega)^{\beta}CPE$, where β is less than or equal to 1. The equation for an equivalent circuit is $Z^* = Z' + iZ''$:

$$Z' = \frac{R_g}{1 + (\omega_g \cdot R_g \cdot C_g)^2} + \frac{R_{gb}}{1 + (\omega_{gb} \cdot R_{gb} \cdot C_{gb})^2} \quad (2)$$

$$Z'' = \frac{\omega_g \cdot R_g \cdot C_g}{1 + (\omega_g \cdot R_g \cdot C_g)^2} + \frac{\omega_{gb} \cdot R_{gb} \cdot C_{gb}}{1 + (\omega_{gb} \cdot R_{gb} \cdot C_{gb})^2} \quad (3)$$

where $(\omega_g \cdot R_g \cdot C_g)$ and $(\omega_{gb} \cdot R_{gb} \cdot C_{gb})$ represent the frequency, resistance and capacitance at the peaks of the semicircles for both the grain and grain boundaries respectively. While the circular arc sections on the Z' axis are used to determine resistance, the following formulas are used to compute capacitance:

$$C_g = \frac{1}{\omega_g \cdot R_g} \quad (4)$$

$$C_{gb} = \frac{1}{\omega_{gb} \cdot R_{gb}} \quad (5)$$

Fitting results (given in Supporting Information[§] in Table S1), showed that with increasing temperature grain boundary resistivity (R_{gb}) becomes greater than grain resistivity (R_g), implying that the conducting component in the samples is passing through the grains. In addition, the resistance of both grain (R_g) and grain boundary (R_{gb}) decreases as temperature increases for all samples. The samples CE3 and 2CE consistently demonstrate higher resistance values, while the CE2 and CE3 samples show a more significant reduction in resistance with increasing temperature, indicating enhanced charge carrier mobility.

3.7. Dielectric dispersion

Figures 11 and 12 show the variation of the real (ε') and imaginary (ε'') components of permittivity at varying temperatures (300–400 °C) over a frequency range of 10^2–10^6 Hz. Both ε' and ε'' have significant values in the low-frequency range, decreasing sharply in lower frequency and gradually in regions of higher frequencies. This behaviour can be explained by dipolar relaxation, where various types of polarizations, such as electronic, dipolar, interfacial and ionic polarisations, contribute to the overall polarization of dielectric materials

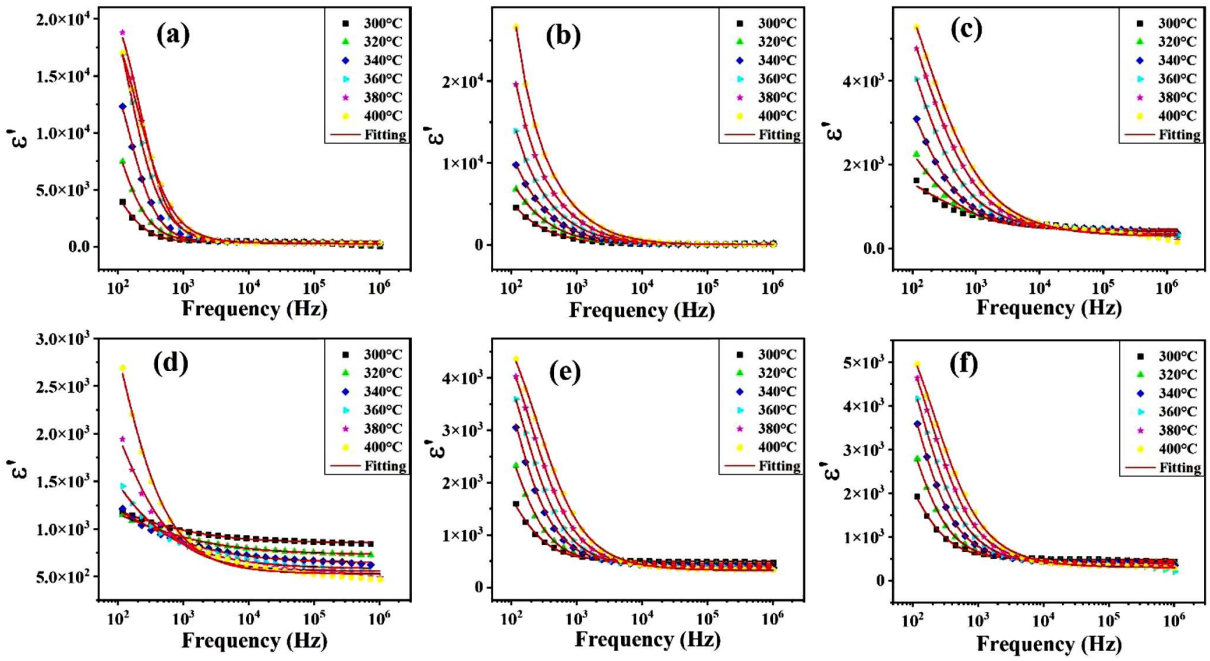

Figure 11. The real part of dielectric constant (ε') versus frequency at different temperature for samples: a) BZT, b) CE, c) CE2, d) CE3, e) 2CE and f) 3CE

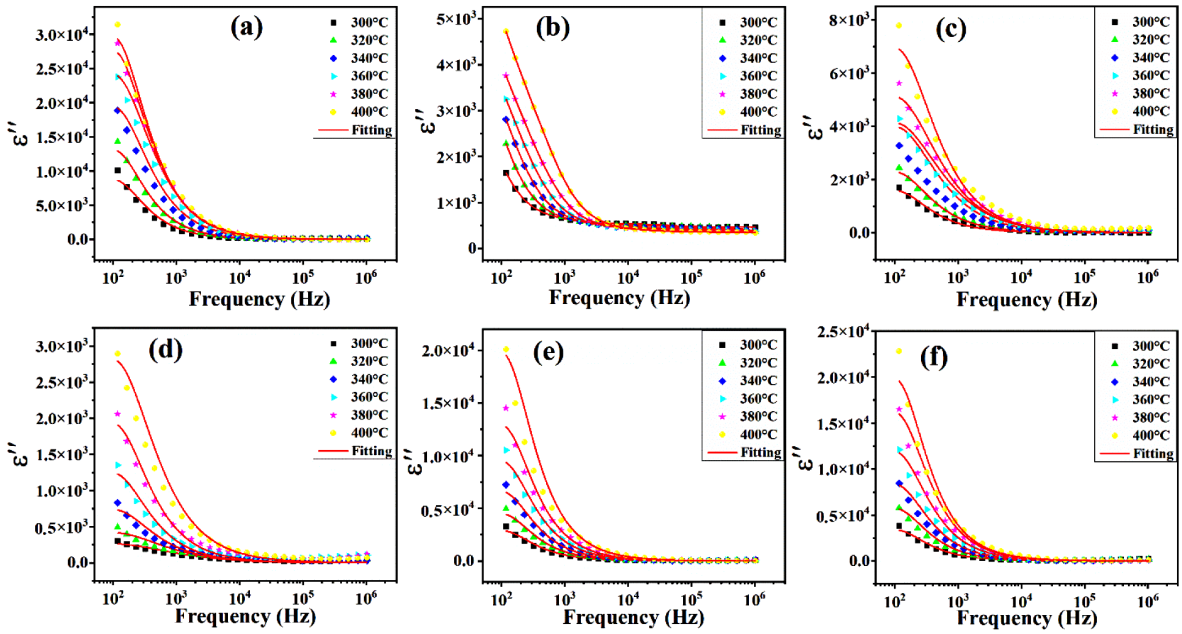

Figure 12. The imaginary part of dielectric constant (ε'') vs. frequency at different temperature for samples: a) BZT, b) CE, c) CE2, d) CE3, e) 2CE and f) 3CE

[62]. All samples have good responses to low-frequency generated electric fields, resulting in high total polarisation and hence high ε' and ε'' values. Despite this, at higher frequencies, certain polarizations do not change per time-dependent electric fields. Therefore, such orientations have low ε' and ε'' values because they do not impact the material's net polarization. With the increase in temperature from 300 to 400 °C, there is an observed rise in the dielectric constant value within the lower frequency range. Figure 11 clearly illustrates that the ε' initially increases with the molar concentration of the dopant and then decreases. This change is more prominent in the case of a higher Er/Cu molar ratio. The abnormal grain size in the different compositions may be responsible for increased dielectric properties. That is, charge carrier transport improves with increasing temperature. In the frequency range under investigation, the addition of Er and Cu dopants in the BZT matrix inhibits the high-frequency relaxation process. This leads to a shift of the relaxation frequency towards higher values and results in a static dielectric constant across a wide frequency range, spanning from 10^4 Hz to 10^6 Hz. This behaviour can be attributed to the limited ability of electric dipoles to quickly respond to rapidly changing electric fields. This leads to increased friction between the dipoles, which may be explained by the presence of different types of polarization within these samples [63–65]. As the value of dielectric constant determines the capacity of a capacitor to store energy when a voltage is applied, the static nature of dielectric constants under a specific frequency window favours the constant amount of energy storage within this frequency range [66].

To understand dielectric relaxation in samples, the Cole-Cole relaxation model was applied [67]. The dielectric data confirm the non-Debye behaviour for all the samples, but more information is given in Supporting Information (Table S2).

3.8. Electric modulus analysis

One significant advantage of the modulus analysis method is its ability to predict the contributions of grain and grain boundaries, particularly at high temperatures, which is unlikely to be achieved using complex impedance graphs. This allows for a more comprehensive understanding of the material's behaviour under different conditions.

The evaluation of dielectric relaxation processes in low-capacitance samples often involves the use of the elastic modulus. This approach allows for the evaluation of the dielectric response exhibited by insulating materials. The complex modulus, consisting of the real part (M') and imaginary part (M''), is especially valuable in studying relaxation phenomena in ceramics [68]. Additionally, this approach enables the analysis of both grain and grain boundaries, particularly at elevated temperatures, a task that is challenging with complex impedance graphs. The formula for the complex modulus is given as:

$$M^*(\omega) = M'(\omega) + iM''(\omega) \tag{6}$$

The plots of the electric modulus (M') versus frequency presented in Fig. 13 demonstrate interesting temperature-dependent trends. As the temperature increases, the M' values continuously shift towards higher frequencies and approach zero in the low-frequency range. This behaviour indicates that induced electric fields have no impact on charge carrier movement since there is no restoring force [57,69]. This observation suggests that charge carriers in the material exhibit short-range mobility during the conduction phenomenon [57].

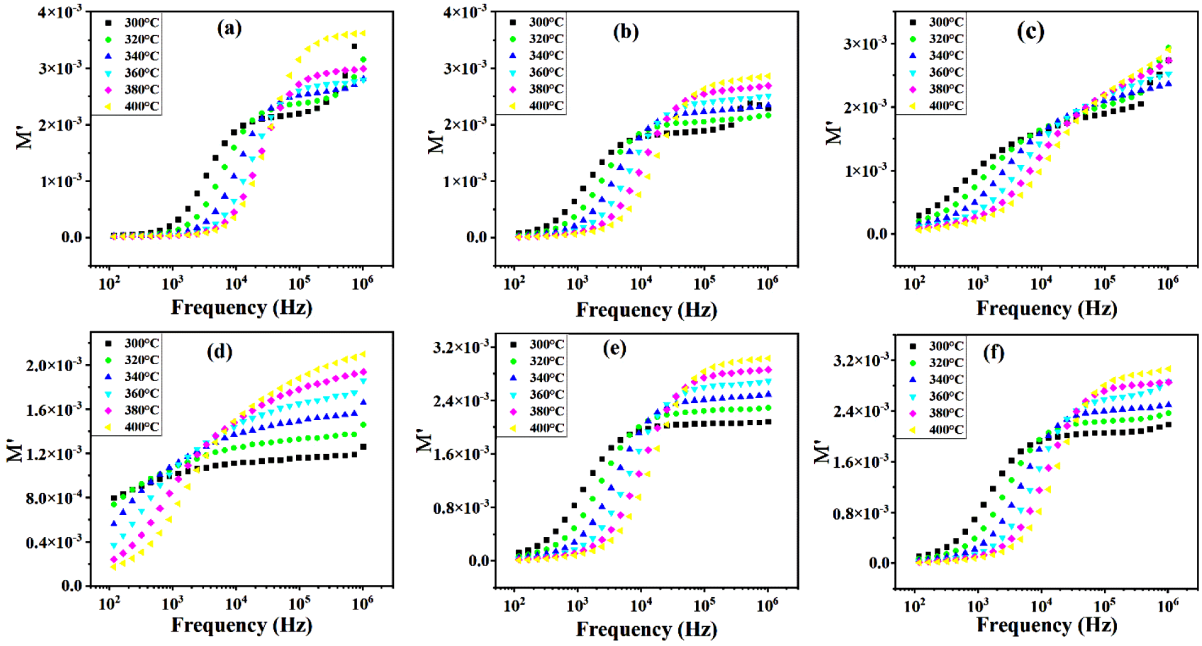

Figure 13. The real part of electrical modulus (M') vs frequency at different temperature for samples: a) BZT, b) CE, c) CE2, d) CE3, e) 2CE and f) 3CE

Figure 14 displays the relationship between the imaginary component of the electrical modulus (M'') and frequency at different temperatures. With increasing temperature, the peak of M'' shifts towards higher frequencies. This indicates that the sample exhibits electrical conduction hopping, which can be attributed to the mixed oxidation state of Ba^{2+} and Er^{3+}. The widening of the asymmetrical modulus peak suggests a non-Debye relaxation type [69,70]. Furthermore, with increasing frequency, the shifting of the peak position indicates a transition from long-range to short-range mobility in the relaxation process. To fit the experimental data, Bergmann's modified Kohlrausch-Williams-Watts (KWW) equation was employed [71,72]:

$$M'' = \frac{M''_{max}}{(1-\alpha) + \frac{\alpha}{1+\alpha}\left[\alpha\frac{\omega_{max}}{\omega} + \left(\frac{\omega}{\omega_{max}}\right)^{\alpha}\right]} \tag{7}$$

where M''_{max} represents the maximum value of M'', ω_{max} is the frequency at which the peak appears and α is fit parameter. As shown in Fig. 15, the experimental data exhibits a reasonable agreement with the fitted theoretical data (see Supporting Information Table S2). Trends of α illustrate that the non-linear coefficient decreases

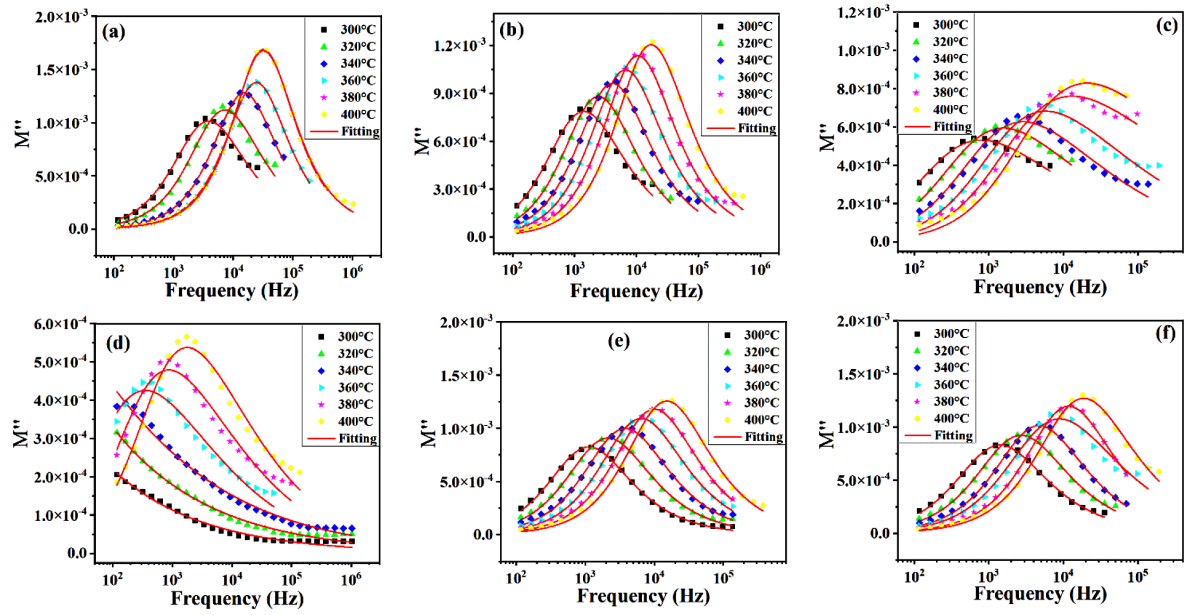

Figure 14. The imaginary part of electrical modulus (M'') vs. frequency at different temperature for samples: a) BZT, b) CE, c) CE2, d) CE3, e) 2CE and f) 3CE

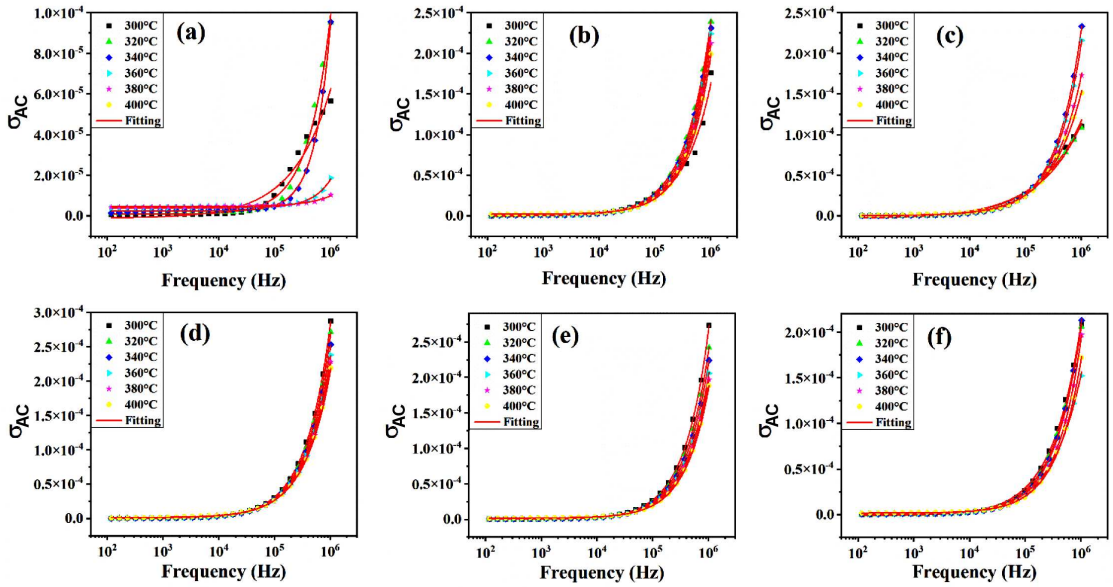

Figure 15. AC conductivity vs. frequency profile at different temperatures for samples: a) BZT, b) CE, c) CE2, d) CE3, e) 2CE and f) 3CE

with an increase in molar concentration of Er, indicating an enhancement in the stretched dielectric phenomenon due to a reduction in space charge polarization.

Overall, the complex modulus analysis provides valuable insights into the dielectric properties and relaxation dynamics of the examined ceramics. These findings contribute to a deeper understanding of the material's behaviour and can guide the design and optimization of dielectric materials for various applications.

3.9. Conductivity assessment

Figure 15 illustrates the correlation between electrical conductivity and frequency across a temperature range of 300 to 400 °C. The AC electrical conductivity (σ_{AC}) can be calculated using the following equation [73]:

$$\sigma_{AC} = 2\pi \cdot \omega \cdot \varepsilon \cdot \varepsilon_0 \cdot \tan\delta \tag{8}$$

which involves the frequency (ω), the permittivity of the material (ε), and the vacuum permittivity (ε_0). The investigation of frequency response on AC conductivity was carried out using Jonscher's universal power law, which is stated as [74]:

$$\sigma_{AC} = \sigma_{DC} + A \cdot \omega^n \tag{9}$$

where A represents a characteristic parameter and n is the temperature and frequency-dependent exponent with values ranging from 0 to 1. A value of n closer to 0 indicates perfect ionic crystals, while a value of n closer to 1 signifies a Debye dielectric dipolar material. Also, A denotes the power of polarization, and n represents interactions between the surrounding lattice and mobile ions [75–77].

Figure 15 shows separate regions of plateau and dispersion. The conductivity plateau region is found to be independent of frequency, indicating DC conductivity, while the dispersion region, which occurs at higher frequencies, exhibits AC conductivity. The frequency at which the electrical conductivity of the ceramic abruptly rises with temperature is referred to as the hopping frequency. As depicted in Fig. 15, the AC conductivity values demonstrate an upward trend with the increasing Er/Cu molar ratio. This is because the impedance data showed an increase in oxygen vacancies:

$$2\,Ba_{Ba}^{*} + 3\,O_O^{*} \longrightarrow 2\,V_{Ba}'' + 3\,V_O^{\bullet\bullet} + Ba_2CO \tag{10}$$

$$Er_2O_3 \longrightarrow 2\,Er_{Ba}'' + 2\,V_O^{\bullet\bullet} + O_O^{*} \tag{11}$$

$$CuO_3 \longrightarrow Cu_{Ti}'' + 2\,V_O^{\bullet\bullet} + O_O^{*} \tag{12}$$

Figure 15 also includes a fit line (red line) obtained using the Jonscher's power law, providing a good simulation of the conduction process. The determination of the conduction mechanism can be facilitated by analysing the values of n. Figure 16 depicts the temperature dependence of n for all samples, aiding in the iden-

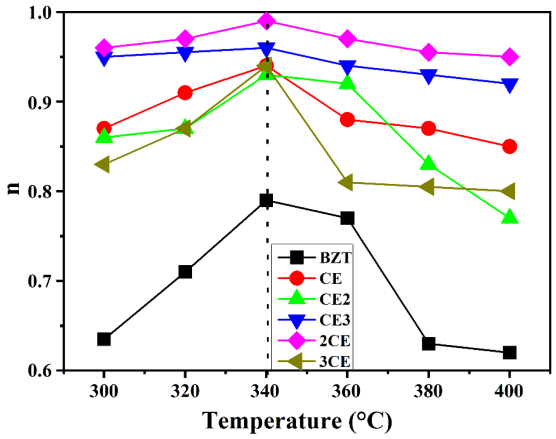

Figure 16. Trend of the exponent n for all the samples

tification of the conduction mechanism. The decrease in n with increasing temperature indicates the application of the correlated barrier hopping (CBH) model. In the case of the overlapping large polaron tunnel (OLPT) conduction model, the exponent n initially decreases as the temperature rises, reaches a minimum value, and then increases with further temperature increase. The quantum mechanical tunnelling (QMT) model maintains a constant n value of 0.8, irrespective of temperature [78]. On the other hand, the small non-overlapping polaron tunnelling (NSPT) model exhibits an increasing n value with temperature. Figure 16 shows that n increases with temperature in the 300 to 340 °C range and then decreases up to 400 °C. This pattern suggests that the NSPT model best explains conduction in the 300 to 340 °C range, while all samples follow the CBH model beyond that temperature range.

Values of σ_{DC} and n derived from the fitting of σ_{AC} with the Jonscher's power law are given in Table S3 (Supporting Information). The conductivity increases with temperature. The undoped BZT ceramics demonstrates higher conductivity values compared to the other samples across all temperature ranges. The ceramics with higher Cu content (the samples, CE, 2CE, and 3CE) exhibit increasing conductivity values in comparison to other doped BZT ceramics. Linear fitting of $\log(\sigma_{DC})$ to $1000/T$, the activation energy values can be determined, as illustrated in Fig. 17. The calculated activation energy for the different samples is within the range of 0.131 eV to 0.169 eV indicating the energy required for charge carriers to move through the material. The observed values of n close to 1 (Table S3 Supporting Information) suggest that ionic conduction dominates in the $BaZr_{0.05}Ti_{0.95}O_3$ system. This aligns with the composition of the material, which consists of metal cations and oxygen anions, allowing for the migration of ions and the conduction of electric current.

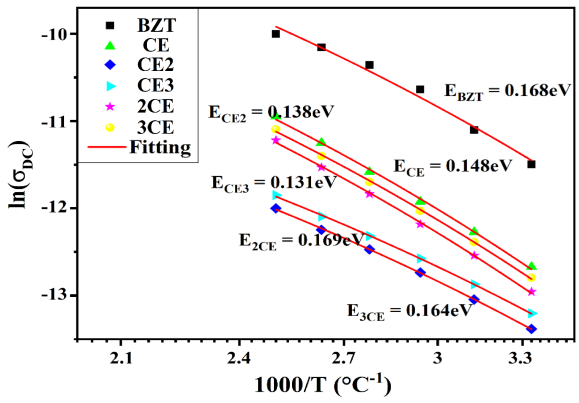

Figure 17. The linear fitting of $\log\sigma_{DC}$ vs. $1000/T$

IV. Conclusions

Cu^{2+} and Er^{3+} doped $BaZr_{0.05}Ti_{0.95}O_3$ ceramics were prepared using the solid-state reaction method, where amount of CuO + Er_2O_3 was fixed at 2 wt.% and different CuO : Er_2O_3 molar ratios (i.e. 1:1, 1:2, 1:3, 2:1 and 3:1) were used. Phase composition was determined using XRD and FTIR analyses and a single phase tetragonal structure with *P*4*mm* symmetry was confirmed for all sintered samples. The Cu^{2+}/Er^{3+} doping resulted in a reduction in grain size and density also caused the increase of dielectric constant and a significant reduction in tangent loss. The dielectric data confirm the non-Debye nature of all the samples. The highest energy storage density of 40.51 mJ/cm^3 with an energy efficiency of 78.8% was obtained in the sample with CuO : Er_2O_3 molar ratio of 2:1. Impedance spectroscopy and electrical modulus studies have demonstrated the contribution of both grains and grain boundaries to conduction. The two types of conduction mechanisms have proven to be present in the systems under the selected temperature range for all the samples. The Arrhenius fitting of DC conductivity gave the values of activation energies in the range of 0.131 eV to 0.169 eV of the prepared samples.

Acknowledgement: The author, Aryan Singh Lather is thankful to UGC (1329/(CSIR-UGC NET Dec.2017) for providing support for the research work.

§ Supplementary data can be downloaded using following link: https://t.ly/OJhYp

References

1. P.K. Panda, "Review : environmental friendly lead-free piezoelectric materials", *J. Mater. Sci.*, **44** (2009) 5049–5062.
2. Y. Liu, A.R. West, "Ho-doped $BaTiO_3$: Polymorphism, phase equilibria and dielectric properties of $BaTi_{1-x}Ho_xO_{3-x/2}$: $0 \le x \le 0.17$", *J. Eur. Ceram. Soc.*, **29** (2009) 3249–3257.
3. S.K. Jo, J.S. Park, Y.H. Han, "Effects of multi-doping of rare-earth oxides on the microstructure and dielectric properties of $BaTiO_3$", *J. Alloys Compd.*, **501** (2010) 259–264.
4. Z. Jiwei, Y. Xi, Z. Liangying, S. Bo, H. Chen, "Thin films grown by a sol-gel process", *Ferroelectrics*, **329** (2005) 23–27.
5. G. Nag Bhargavi, T. Badapanda, A. Khare, M. Shahid Anwar, N. Brahme, "Investigation of structural and conduction mechanism of Europium modified $BaZr_{0.05}Ti_{0.95}O_3$ ceramic prepared by solid-state reaction method", *Appl. Phys. A Mater. Sci. Process.*, **127** (2021) 528.
6. Y. Tsur, T.D. Dunbar, C.A. Randall, "Crystal and defect chemistry of rare earth cations in $BaTiO_3$", *J. Electroceram.*, **7** (2001) 25–34.
7. B.D. Stojanovic, C.R. Foschini, V.B. Pavlovic, V.M. Pavlovic, V. Pejovic, J.A. Parela, "Barium titanate screen-printed thick films", *Ceram. Int.*, **28** (2002) 293–298.
8. X.G. Tang, H. L.W. Chan, A.L. Ding, "Structural, dielectric and optical properties of Ba(Ti, Zr)O_3 thin films prepared by chemical solution deposition", *Thin Solid Films*, **460** (2004) 227–231.
9. Z. Yu, C. Ang, R. Guo, A.S. Bhalla, "Dielectric properties and high tunability of $Ba(Ti_{0.7}Zr_{0.3})O_3$ ceramics under dc electric field", *Appl. Phys. Lett.*, **81** (2002) 1285–1287.
10. U. Weber, G. Greuel, U. Boettger, S. Weber, D. Hennings, R. Waser, "Dielectric properties of Ba(Zr,Ti)O_3-based fer-

roelectrics for capacitor applications", *J. Am. Ceram. Soc.*, **84** (2001) 759–766.
11. S. Miao, J. Pokorny, U.M. Pasha, O.P. Thakur, D.C. Sinclair, I.M. Reaney, "Polar order and diffuse scatter in $BaTi_{1-x}Zr_xO_3$", *J. Appl. Phys.*, **106** (2009) 114111.
12. A. Dixit, S.B. Majumder, A. Savvinov, R.S. Katiyar, R. Guo, A.S. Bhalla, "Investigations on the sol-gel-derived barium zirconium titanate thin films", *Mater. Lett.*, **56** (2002) 933–940.
13. S. Yan, Z. Zhang, Y. Li, Y. Wang, "Effect of internal stresses on temperature-dependent dielectric properties of Fe-doped BZT ceramics", *Ceram. Int.*, **43** (2017) 12605–12608.
14. A.S. Džunuzović, M.M. Vijatović Petrović, J.D. Bobić, N.I. Ilić, B.D. Stojanović, "Magnetoelectric properties of materials based on barium zirconium titanate and various magnetic compounds", *Process. Appl. Ceram.*, **15** [3] (2021) 256–269.
15. L. Curecheriu, T. Sandu, O. Condurache, G. Canu, C. Costa, M.T. Buscaglia, M. Asandulesa, J. Banys, V. Buscaglia, M. Mitoseriu, "Dielectric, ferroelectric and electrocaloric properties of 1%Eu - doped $BaZr_yTi_{1-y}O_3$ ceramics", *Mater. Res. Bull.*, **157** (2023) 112034.
16. A.K. Kalyani, A. Senyshyn, R. Ranjan, "Polymorphic phase boundaries and enhanced piezoelectric response in extended composition range in the lead free ferroelectric $BaTi_{1-x}Zr_xO_3$", *J. Appl. Phys.*, **114** (2013) 014102.
17. W. Li, Z. Xu, R. Chu, P. Fu, G. Zang, "Dielectric and piezoelectric properties of $Ba(Zr_xTi_{1-x})O_3$ lead-free ceramics", *Brazilian J. Phys.*, **40** (2010) 353–356.
18. T. Badapanda, S. Chaterjee, A. Mishra, R. Ranjan, S. Anwar, "Electric field induced strain, switching and energy storage behaviour of lead free Barium Zirconium Titanate ceramic", *Phys. B Condens. Matter*, **521** (2017) 264–269.
19. P.A. Jha, A.K. Jha, "Enhancement in electrical properties and blue emission due to nanostructuring of $BaZr_{0.05}Ti_{0.95}O_3$ ferroelectric ceramics", *J. Mater. Sci. Mater. Electron.*, **25** [2] (2014) 797–804.
20. S. Mahajan, O. P. Thakur, D.K. Bhattacharya, K. Sreenivas, "Ferroelectric relaxor behaviour and impedance spectroscopy of Bi_2O_3-doped barium zirconium titanate ceramics", *J. Phys. D. Appl. Phys.*, **42** (2009) 065413.
21. Z. Yu, C. Ang, R. Guo, A.S. Bhalla, "Dielectric properties of $Ba(Ti_{1-x}Zr_x)O_3$ solid solutions", *Mater. Lett.*, **61** (2007) 326–329.
22. H. Feng, J. Hou, Y. Qu, D. Shan, G. Yao, "Structure, dielectric and electrical properties of cerium doped barium zirconium titanate ceramics", *J. Alloys Compd.*, **512** (2012) 12–16.
23. L. Yuanliang, C. Zhimin, S. Rongli, M. Xuegang, "Microstructure and dielectric behaviour of ytterbium doped $BaZr_{0.1}Ti_{0.9}O_3$ ceramic", *Mater. Res.*, **19** (2016) 1376–1380.
24. J.Q. Qi, B.B. Liu, H.Y. Tian, H. Zou, Z.X. Yue, L.T. Li, "Dielectric properties of barium zirconate titanate (BZT) ceramics tailored by different donors for high voltage applications", *Solid State Sci.*, **14** (2012) 1520–1524.
25. X. Chou, J. Zhai, H. Jiang, X. Yao, "Dielectric properties and relaxor behavior of rare-earth (La, Sm, Eu, Dy, Y) substituted barium zirconium titanate ceramics", *J. Appl. Phys.*, **102** (2007) 084106.
26. T. Badapanda, S. Sarangi, B. Behera, S. Anwar, T.P. Sinha, R. Ranjan, G.E. Luz Jr., E. Longo, L.S. Cavalcante, "Structural refinement, optical and electrical properties of $(Ba_{1-x}SM_{2/3})(Zr_{0.05}Ti_{0.95})O_3$ ceramics", *J. Mater. Sci. Mater. Electron.*, **25** (2014) 3427–3439.
27. S.K. Ghosh, S.K. Rout, S.K. Deshpande, "Structural and scaling behavior in relaxor ferroelectric BZT ceramic doped with rare earth europium ion", *Jt. IEEE Int. Symp. Appl. Ferroelectr. Int. Symp. Integr. Funct. Piezoelectric Force Microsc. Work. ISAF/ISIF/PFM 2015*, **3** (2015) 17–20.
28. D. Sitko, W. Bąk, B. Garbarz-Glos, A. Kulińska, M. Antonova, A. Kalvane, W. Śmiga, "Study of the dielectric properties of europium doped barium titanate ceramics by an impedance spectroscopy", *Ferroelectrics*, **485** (2015) 58–62.
29. S. Halder, T. Schneller, R. Waser, F. Thomas, "Microstructure and electrical properties of $(Ba,Sr)TiO_3$ferroelctric thin films on nickel electrodes", *J. Sol-Gel Sci. Technol.*, **42** (2007) 203–207.
30. A. Rached, M.A. Wederni, A. Belkahla, J. Dahri, K. Khirouni, S. Alaya, R.J. Martín-Palma, "Effect of doping in the physico-chemical properties of $BaTiO_3$ ceramics", *Phys. B Condens. Matter*, **596** (2020) 412343.
31. T. Nakamura, K. Homma, K. Tachibana, "Impedance spectroscopy of manganite films prepared by metalorganic chemical vapor deposition", *J. Nanosci. Nanotechnol.*, **11** (2011) 8408–8411.
32. A. Shukla, R.N.P. Choudhary, "High-temperature impedance and modulus spectroscopy characterization of La^{3+}/Mn^{4+} modified $PbTiO_3$ nanoceramics", *Phys. B Condens. Matter*, **406** (2011) 2492–2500.
33. A. Outzourhit, M.A.E.I. Raghni, M.L. Hafid, F. Bensamka, "Dielectric characterization of hydrothermally prepared.", *Moroccan Stat. Phys. Condens. Matter Soc.,* **8** (2007) 83–87.
34. M. Viviani, M.T. Buscaglia, V. Buscaglia, L. Mitoseriu, A. Testino, P. Nanni, D. Vladikova, "Analysis of conductivity and PTCR effect in Er-doped $BaTiO_3$ ceramics", *J. Eur. Ceram. Soc.*, **24** (2004) 1221–1225.
35. G. Dale, M. Conway, M. Strawhorne, J. McLaughlin, "An Investigation into the electrical properties of doped barium Titanate using electrical impedance spectroscopy (EIS)", *Ferroelectrics*, **448** (2013) 50–57.
36. A. Shukla, R.N.P. Choudhary, A.K. Thakur, D.K. Pradhan, "Structural, microstructural and electrical studies of La and Cu doped $BaTiO_3$ ceramics", *Phys. B Condens. Matter*, **405** (2010) 99–106.
37. K. Zhang, X. Liu, N. Bai, Z. Li, Q. Wu, Z. Yang, "Modification of $(Zr_{0.8}Sn_{0.2})TiO_4$ high-frequency dielectric ceramics doped with CuO-TiO_2" *J. Mater. Sci.: Mater. Electron.*, **32** (2021) 4090–4096.
38. C. Zhao, H. Wang, J. Xiong, J. Wu, "Composition-driven phase boundary and electrical properties in $(Ba_{0.94}Ca_{0.06})(Ti_{1-x}M_x)O_3$ (M = Sn, Hf, Zr) lead-free ceramics", *Dalt. Trans.*, **45** (2016) 6466–6480.
39. N. Ding, X.G. Tang, X.D. Ding, Q.X. Liu, Y.P. Jiang, L.L. Jiang, "Effect of Zr/Ti ratio on the dielectric and piezoelectric properties of Mn-doped $Ba(Zr,Ti)O_3$ ceramics", *J. Mater. Sci. Mater. Electron.*, **25** (2014) 2305–2310.
40. M. Wang, R. Zuo, S. Qi, L. Liu, "Synthesis and characterization of sol-gel derived $(Ba,Ca)(Ti,Zr)O_3$ nanoparticles", *J. Mater. Sci. Mater. Electron.*, **23** (2012) 753–757.
41. S. Utara, S. Hunpratub, "Ultrasonic assisted synthesis of $BaTiO_3$ nanoparticles at 25 °C and atmospheric pressure",

Ultrason. Sonochem., **41** (2018) 441–448.
42. S.J. Chang, W.S. Liao, C.J. Ciou, J.T. Lee, C.C. Li, "An efficient approach to derive hydroxyl groups on the surface of barium titanate nanoparticles to improve its chemical modification ability", *J. Colloid Interface Sci.*, **329** (2009) 300–305.
43. S.R. Teeparthi, E.W. Awin, R. Kumar, "Dominating role of crystal structure over defect chemistry in black and white zirconia on visible light photocatalytic activity", *Sci. Rep.*, **8** (2018) 5541.
44. M.H. Zare, A. Mehrabani-Zeinabad, "Photocatalytic activity of $ZrO_2/TiO_2/Fe_3O_4$ ternary nanocomposite for the degradation of naproxen: characterization and optimization using response surface methodology", *Sci. Rep.*, **12** (2022) 10388.
45. S.K. Sinha, S.N. Choudhary, R.N. Choudhary, "Structural, electrical and dielectric behavior of $Pb(Mg_{1/4}Ni_{1/4}W_{1/2})O_3$ ceramics", *J. Electroceramics*, **3** (2002) 121–126.
46. R.E. Cohen, "Origin of ferroelectricity in perovskite oxides", *Nature,* **358** (1992) 136–138.
47. A.S. Lather, K. Poonia, R.S. Kundu, N. Ahlawat, A. Nehra, S. Kaur, "Assessment of conductivity through impedance analysis of $CuO:Ho_2O_3$ modified $BaZr_{0.05}Ti_{0.95}O_3$", *ECS J. Solid State Sci. Technol.*, **12** (2023) 093013.
48. A.S. Kumar, C.S.C. Lekha, S. Vivek, V. Saravanan, K. Nandakumar, S.S. Nair, "Multiferroic and magnetoelectric properties of $Ba_{0.85}Ca_{0.15}Zr_{0.1}Ti_{0.9}O_3$–$CoFe_2O_4$ core-shell nanocomposite", *J. Magn. Magn. Mater.*, **418** (2016) 294–299.
49. T. Badapanda, S. Sarangi, B. Behera, P.K. Sahoo, S. Anwar, T.P. Sinha, G.E. Luz Jr., E. Longo, L.S. Cavalcante, "Structural refinement, optical and ferroelectric properties of microcrystalline $Ba(Zr_{0.05}Ti_{0.95})O_3$ perovskite", *Curr. Appl. Phys.*, **14** (2014) 708–715.
50. H. Sun, Y. Zhang, X. Liu, Y. Liu, W. Chen, "Effects of CuO additive on structure and electrical properties of low-temperature sintered $Ba_{0.98}Ca_{0.02}Zr_{0.02}Ti_{0.98}O_3$ lead-free ceramics", *Ceram. Int.*, **41** (2015) 555–565.
51. T. Badapanda, S. Sarangi, B. Behera, S. Anwar, "Structural and impedance spectroscopy study of samarium modified barium zirconium titanate ceramic prepared by mechanochemical route", *Curr. Appl. Phys.*, **14** (2014) 1192–1200.
52. U. Dash, S. Sahoo, P. Chaudhuri, S.K.S. Parashar, K. Parashar, "Electrical properties of bulk and nano Li_2TiO_3 ceramics: A comparative study", *J. Adv. Ceram.*, **3** (2014) 89–97.
53. B. Tiwari, R.N.P. Choudhary, "Study of impedance parameters of cerium modified lead zirconate titanate ceramics", *IEEE Trans. Dielectr. Electr. Insul.*, **17** (2010) 5–17.
54. B. Tiwari, R.N.P. Choudhary, "Frequency-temperature response of $Pb(Zr_{0.65-x}Ce_xTi_{0.35})O_3$ ferroelectric ceramics", *IEEE Trans. Dielectr. Electr. Insul.,* **493** (2010) 1–10.
55. H. Singh, A. Kumar, K.L. Yadav, "Structural, dielectric, magnetic, magnetodielectric and impedance spectroscopic studies of multiferroic $BiFeO_3$–$BaTiO_3$ ceramics", *Mater. Sci. Eng. B*, **176** (2011) 540–547.
56. Y.M. Li, R.H. Liao, X.P. Jiang, Y.P. Zhang, "Impedance spectroscopy and dielectric properties of $Na_{0.5}Bi_{0.5}TiO_3$-$K_{0.5}Bi_{0.5}TiO_3$ ceramics", *J. Alloys Compd.*, **484** (2009) 961–965.
57. R. Ranjan, R. Kumar, B. Behera, R.N.P. Choudhary, "Structural and impedance spectroscopic studies of samarium modified lead zirconate titanate ceramics", *Phys. B Phys. Condens. Matter*, **404** (2009) 3709–3716.
58. M.R. Biswal, J. Nanda, N.C. Mishra, S. Anwar, A. Mishra, "Dielectric and impedance spectroscopic studies of multiferroic $BiFe_{1-x}Ni_xO_3$", *Adv. Mater. Lett.,* **5** (2014) 531–537.
59. S. Sen, R.N. Choudhary, "Impedance studies of Sr modified $BaZr_{0.05}Ti_{0.95}O_3$ ceramics", *Mater. Chem. Phys.*, **87** (2004) 256–263.
60. R. Kaur, V. Sharma, M. Kumar, M. Singh, A. Singh, "Conductivity relaxation in $Pb_{0.9}Sm_{0.10}Zr_{0.405}Ti_{0.495}Fe_{0.10}O_3$ solid solution", *J. Alloys Compd.*, **735** (2018) 1472–1479.
61. V. Sharma, R. Kaur, M. Singh, R. Selvamani, S.M. Gupta, V.S. Tiwari, A.K. Karnal, "Conductivity relaxation and oxygen vacancies-related electron hopping mechanism in $Pb_{1-x}La_{x/2}Sm_{x/2}Ti_{1-x}Fe_xO_3$ solid solutions", *J. Asian Ceram. Soc.*, **6** (2018) 222–231.
62. M. Kumar, K.L. Yadav, "Study of dielectric, magnetic, ferroelectric and magnetoelectric properties in the $PbMn_xTi_{1-x}O_3$ system at room temperature", *J. Phys. Condens. Matter*, **19** (2007) 1–7.
63. M. Rawat, K.L. Yadav, "Study of structural, electrical, magnetic and optical properties of $0.65BaTiO_3$–$0.35Bi_{0.5}Na_{0.5}TiO_3$–$BiFeO_3$ multiferroic composite", *J. Alloys Compd.*, **597** (2014) 188–199.
64. Z. Yu, C. Ang, "Maxwell-Wagner polarization in ceramic composites $BaTiO_3$–$Ni_{0.3}Zn_{0.7}Fe_{2.1}O_4$", *J. Appl. Phys.*, **91** (2002) 794–797.
65. M.A. Ahmed, S.T. Bishay, G. Abdelatif, "Effect of ytterbium on the electrical properties of Li-Co ferrite", *J. Phys. Chem. Solids*, **62** (2001) 1039–1046.
66. C.T. Black, J.J. Welser, "Electric-field penetration into metals: consequences for high-dielectric-constant capacitors", *IEEE Trans. Electron Devices*, **46** (1999) 776–780.
67. P.R. Mason, J.B. Hasted, L. Moore, "The use of statistical theory in fitting equations to dielectric dispersion data", *Adv. Mol. Relax. Process.*, **6** (1974) 217–232.
68. E. Barsoukov, J.R. Macdonald, *Impedance Spectroscopy Theory, Experiment, and Applications*, 2nd edn. Wiley-Interscience, **14** (2005).
69. Priyanka, A.K. Jha, "Electrical characterization of zirconium substituted barium titanate using complex impedance spectroscopy", *Bull. Mater. Sci.*, **36** (2013) 135–141.
70. T. Badapanda, L.S. Cavalcante, G.E. Luz Jr., N.C. Batista, S. Anwar, E. Longo, "Effect of yttrium doping in barium zirconium titanate ceramics: A structural, impedance, and modulus spectroscopy study", *Metall. Mater. Trans. A Phys. Metall. Mater. Sci.*, **44** (2013) 4296–4309.
71. N. Ortega, A. Kumar, P. Bhattacharya, S.B. Majumder, R.S. Katiyar, "Impedance spectroscopy of multiferroic $PbZr_xTi_{1-x}O_3/CoFe_2O_4$ thin films", *Phys. Rev. B*, **77** (2008) 014111.
72. R. Bergman, "General susceptibility functions for relaxation in disordered functions", *J. Appl. Phys.*, **88** (2000) 1356–1365.
73. V. Prakash, S.N. Choudhary, T.P. Sinha, "Dielectric relaxation in complex perovskite oxide $BaCo_{1/2}W_{1/2}O_3$", *Phys. B*, **403** (2008) 103–108.
74. A.K. Jonscher, "The 'universal' dielectric response", *Nature*, **267** (1977) 673–679.
75. D.K. Pradhan, B. Behera, P.R. Das, "Studies of dielec-

tric and electrical properties of a new type of complex tungsten bronze electroceramics", *J. Mater. Electron.*, **23** (2012) 779–785.

76. S. Pattanayak, R.N.P. Choudhary, P.R. Das, "Effect of Gd-substitution on phase transition and conduction mechanism of $BiFeO_3$", *J. Mater. Sci. Mater. Electron.*, **24** (2013) 2767–2771.
77. G. Catalan, J.F. Scott, "Physics and application of bismuth ferrite", *Adv. Mater.*, **21**(2009) 2463–2485.
78. A. Ghosh, "Frequency-dependent conductivity in bismuth-vanadate glassy semiconductors", *Phys. Rev. B*, **41**(1990) 1479–1488.